Journal Pre-proof


# In vitro pulsatile flow study in compliant and rigid ascending aorta phantoms by stereo particle image velocimetry

Sina G. Yazdi , Paul D. Docherty , Petra N. Williamson , Mark Jermy , Natalia Kabaluik , Adib Khanafer , Patrick H. Geoghegan

PII: S1350-4533(21)00100-4
DOI: https://doi.org/10.1016/j.medengphy.2021.08.010
Reference: JJBE 3700

To appear in: *Medical Engineering and Physics*

Received date: 5 March 2021
Revised date: 5 August 2021
Accepted date: 31 August 2021

Please cite this article as: Sina G. Yazdi , Paul D. Docherty , Petra N. Williamson , Mark Jermy , Natalia Kabaluik , Adib Khanafer , Patrick H. Geoghegan , In vitro pulsatile flow study in compliant and rigid ascending aorta phantoms by stereo particle image velocimetry, *Medical Engineering and Physics* (2021), doi: https://doi.org/10.1016/j.medengphy.2021.08.010

# In vitro pulsatile flow study in compliant and rigid ascending aorta phantoms by stereo particle image velocimetry

*Sina G. Yazdi[1], Paul D. Docherty[1], Petra N. Williamson[1], Mark Jermy[1], Natalia Kabaluik[1], Adib Khanafer[2,3], Patrick H. Geoghegan[4,5]*

1. Department of Mechanical Engineering, University of Canterbury, Private Bag 4800, Christchurch, New Zealand
2. Vascular, Endovascular, & Renal Transplant Unit Christchurch Hospital, Canterbury District Health Board, Riccarton Avenue, Christchurch 8053, New Zealand
3. Christchurch School of Medicine, University of Otago, New Zealand
4. Department of Mechanical, Biomedical and Design, College of Engineering and Physical Sciences Aston University, Birmingham, B4 7ET, England
5. Department of Mechanical and Industrial Engineering, University of South Africa, Johannesburg, South Africa

Corresponding Author: Patrick H Geoghegan

Email: p.geoghegan@aston.ac.uk
Address: College of Engineering and Physical Sciences (EPS),
Department of Mechanical, Biomedical and Design
Aston University
Aston Triangle
Birmingham
B4 7ET, UK
Phone: +44 (0)121 204 5452

**Highlights**

- Particle image velocimetry results demonstrated the necessity of compliance in any haemodynamic study.
- Introduction of compliance into the study of aorta haemodynamics demonstrated and increase in flow recirculation
- a direct correlation was made between the observed recirculation and high-risk areas for atherosclerosis

## Abstract

The aorta is a high risk region for cardiovascular disease (CVD). Haemodynamic patterns leading to CVD are not well established despite numerous experimental and numerical studies. Most overlook effects of arterial compliance and pulsatile flow. However, rigid wall assumptions can lead to overestimation of wall shear stress; a key CVD determinant. This work investigates the effect of compliance on aortic arch haemodynamics experiencing pulsatility. Rigid and compliant phantoms of the arch and brachiocephalic branch (BCA) were manufactured. Stereoscopic particle image velocimetry was used to observe velocity fields. Higher velocity magnitude was observed in the rigid BCA during acceleration. However, during deceleration, the compliant phantom experienced higher velocity. During deceleration, a low velocity region initiated and increased in size in the BCA of both phantoms with irregular shape in the compliant. At mid-deceleration, considerably larger recirculation was observed under compliance compared to rigid. Another recirculation region formed and increased in size on the inner wall of the arch in the compliant during late deceleration, but not rigid. The recirculation regions witnessed identify as high risk areas for atherosclerosis formation by a previous *ex-vivo* study. The results demonstrate necessity of compliance and pulsatility in haemodynamic studies to obtain highly relevant clinical outcomes.

Key terms: Aortic Arch; Compliance; Pulsatile flow; Particle Image velocimetry; Haemodynamics; Cardiovascular Disease;

# 1. Introduction

Cardiovascular disease (CVD) is the leading cause of death with 17.7 million mortalities each year globally [1]. Initiation and development of CVD can be caused by abnormal haemodynamic behaviour. In healthy arteries, endothelial cells regulate the vascular muscle tone by releasing mediator molecules such as nitric oxide (NO) to maintain wall shear stress (WSS) within a certain healthy range [2]. However, WSS fluctuation is a haemodynamic risk factor for CVD [3]. WSS regulates the growth of endothelium cells that constitute the lining of the arterial lumen and abnormal WSS can cause endothelium cell dysfunction [4]. Assemat, Siu [5] noted particular high risk regions for stenosis development including the inlets of the efferent arteries and the distal curvature of the aortic arch lumen (Figure 1). Recirculation has been noted as a risk factor for the development of stenosis [6-8]. Since WSS is directly proportional to velocity gradient at the wall, correctly predicting any adverse velocity profiles is imperative to ensuring that cardiovascular investigations produce relevant data. This paper demonstrates assumptions of rigid boundary conditions in the aortic arch will lead to a misrepresentation of important flow field phenomena and incorrect prediction of the onset of recirculation.



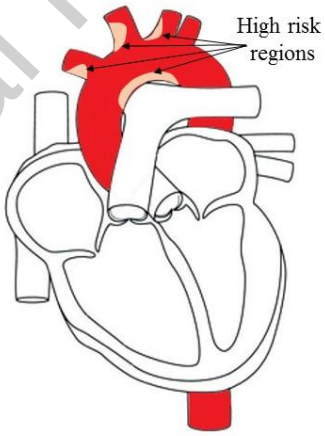


***Fig. 1*** *Danger zones for stenosis formation according to Assemat, Siu [5]*

Healthy and diseased haemodynamics in the aortic arch are not well understood. Numerical and experimental methods have been used to investigate aortic haemodynamics and provide better understanding of disease states and therapeutic procedures [9, 10]. Computational fluid dynamics (CFD) packages have been utilised to simulate healthy and diseased haemodynamics [11-13]. However, numerical studies that lack physical validation provide limitied authority to formulate strong recommandations for CVD treatments.

Therefore, *in-vitro* measurment of haemodynamics using flow phantoms, *ex-vivo* vessels in retrospective patient data, or other haemodynamic measurment should be carried out to validate findings of CFD based haemodynamic research [14].

Several *in-vitro* measurements have been performed on different arterial regions [15-20]. However, these studies were typically performed using rigid arterial phantoms. Studies have shown that rigid assumptions in straight phantoms representing arteries demonstrate WSS overestimation of up to 60% in comparison to compliant models [21-24]. While compliant models of complex geometry are difficult to produce [25], it is imperative they are able to replicate and capture any major elements of haemodynamic behaviour if a model is intended to inform therapy. In particular, changes in the fluid-boundary interaction must be captured to ensure an accurate representation of the biological system. A full review of rigid and compliant phantom fabrication methods and associated difficulties can be found in Yazdi, Geoghegan [25].

This paper presents a haemodynamic study in an idealized, compliant phantom of the ascending aorta and one superior branch. Pulsatile flow fields were evaluated in the phantom using stereoscopic particle image velocimetry technique (SPIV). Particular attention was focussed on regions that have been noted as high risk points for stenosis formation. The results of the study presented in this paper clearly show flow recirculation zones in the compliant model that are not observed in the rigid. These occur in regions classified as danger zones [5]. This is clear evidence that applying rigid wall assumptions will not correctly predict flow phenomena in regions important to cardiovascular disease progression.

## 2. Materials and Methods

The idealized dimensions of the aortic arch with the brachiocephalic artery (BCA) were obtained from a meta-analysis of reported aortic arch geometric parameters [26]. An idealized phantom geometry (Figure 2a) was designed in SolidWorks (SolidWorks, Concord, MA, USA). Two phantoms were used in this analysis: the first was sufficiently stiff to be considered rigid, while the second was thin walled and compliant. The phantoms were designed at 1.5 times life size. The compliant phantom was manufactured from Dow Corning Sylgard 184 silicone, which has a Youngs modulus of 1.32 MPa as previously reported through tensile testing in Geoghegan, Buchmann [27] and the thin walled phantom wall-thickness was modulated to achieve equivalent compliance (31.25×10-6 $Pa^{-1}$) to *in-vivo* conditions [28]. *In-vivo* compliance was matched using the normalised compliance equation (Eq 1) [25].

$$C = \frac{dA}{A_{min} \times dP} = \frac{2\pi r^3}{A_{min} E h} \qquad (1)$$

Where $r$ is the radius, $A_{min}$ is the cross-sectional area of the lumen at zero transmural pressure, $E$ is the modulus of elasticity, and $h$ is the wall thickness of the phantom. The phantoms were fabricated using lost-core casting of silicone [27]. An UP Box (Tiertime, Beijing, China) FDM (fused deposition modelling) 3D printer used an ABS material to print male moulds for the rigid and compliant phantoms.

For the rigid phantom (Figure 2b) the male mould was placed in a PMMA casting box, which was then filled with silicone. After the silicone cured, acetone was used to dissolve the ABS core, leaving the phantom. The compliant phantom fabrication has been detailed in Yazdi, Huetter [29]. A two-piece female mould was 3D printed with dowels were used to locate the male mould centrally in the female mould. Silicone was injected into the cavity between moulds and left to cure. The female mould was mechanically removed from the phantom and the male mould dissolved from the phantom core yielding a phantom with a uniform 1mm wall thickness (Figure 2c).

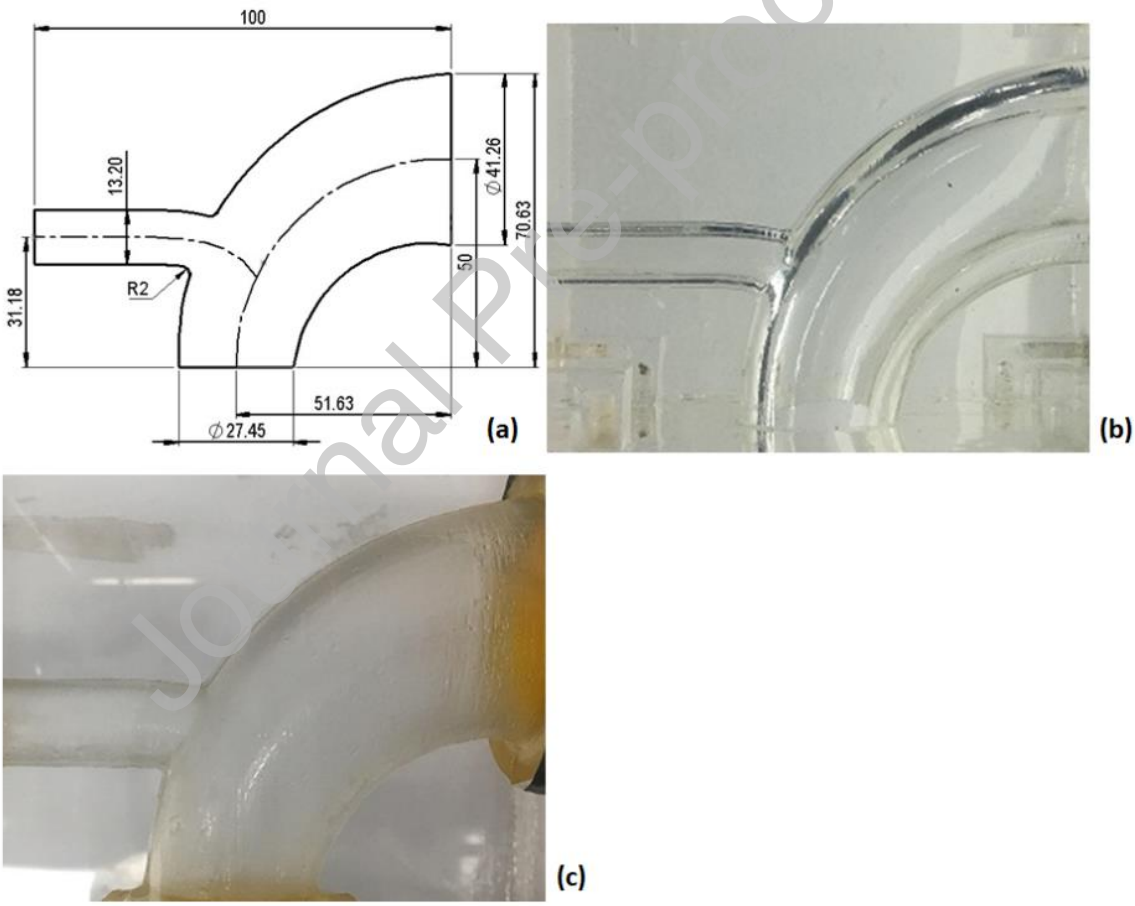


***Fig. 2*** *(a) Schematic drawing of the phantom; dimensions in mm (b) Rigid Phantom (c) Compliant Phantom.*

An aqueous-glycerine mixture was used as the working fluid to mimic blood flow within the phantoms. The refractive index of the working fluid was matched to cured Sylgard 184 (n = 1.417) by defining the ratio of water to glycerine, 39:61 [23]. This effectively eliminated

significant optical distortion caused by the curvature of the phantom [27]. The modulus of elasticity for cured Sylgard was 1.32 MPa and allowed phantom compliance to be matched to that of the human aorta by controlling the wall thickness [28].

The compliant phantom was placed in a compliance chamber filled with the same working fluid. To control the pressure external to the phantom and mimic transmural pressure *in-vivo*, a 160 mm head was applied to the working fluid surrounding the phantom (Figure 3). An in-house developed computer controlled stepper-motor driven reciprocating piston pump induced a physiological flowrate waveform [30] and pumped the working fluid through the phantoms. The pump incorporated a high resolution stepper motor (200 steps per revolution), ball screw, piston and cylinder. The piston rod was connected to a ball screw supported by bearings at the free and motorised ends. The stepper motor was controlled using a Labview programme via a National Instruments 9401 digital module and 9172 Compact DAQ chassis using feedback control.

To match physiological conditions across the change in diameter and working fluid kinematic viscosity (ν), the flow rates of the working fluid were scaled to match the *in-vivo* Reynolds (Re– Eq.2) and Womersley numbers (α– Eq.3) using the proximal diameter (41.26 mm) as the characteristic length (L) [28]. The kinematic viscosity of the water-glycerine mixture was 9.3 x $10^{-6}$ $m^2/s$. Figure 4a shows the *in-vitro* inlet flow waveform. The outlet flow conditions were maintained by a constant pressure head with a weir placed 160 mm above the inlet level. The Womersley number was 9.7 and the maximum Reynolds numbers was 1220 [31].

$$Re = \frac{UL}{\nu} \qquad (2)$$

$$\alpha = \frac{L}{2}\sqrt{\frac{\omega}{\nu}} \qquad (3)$$

Where U is velocity and ω is angular frequency.

The flow circuit consisted of the pump, a flow straightener, electromagnetic flowmeter (IFC 300 KROHNE Ltd, UK, located directly upstream of the entrance to the phantom, providing a real-time output of the entrance waveform), the phantom with two outlets and a header tank. Impedance of the capillary network was mimicked by the header tank. A weir in the header tank maintained a constant outlet pressure head (Figure 3).

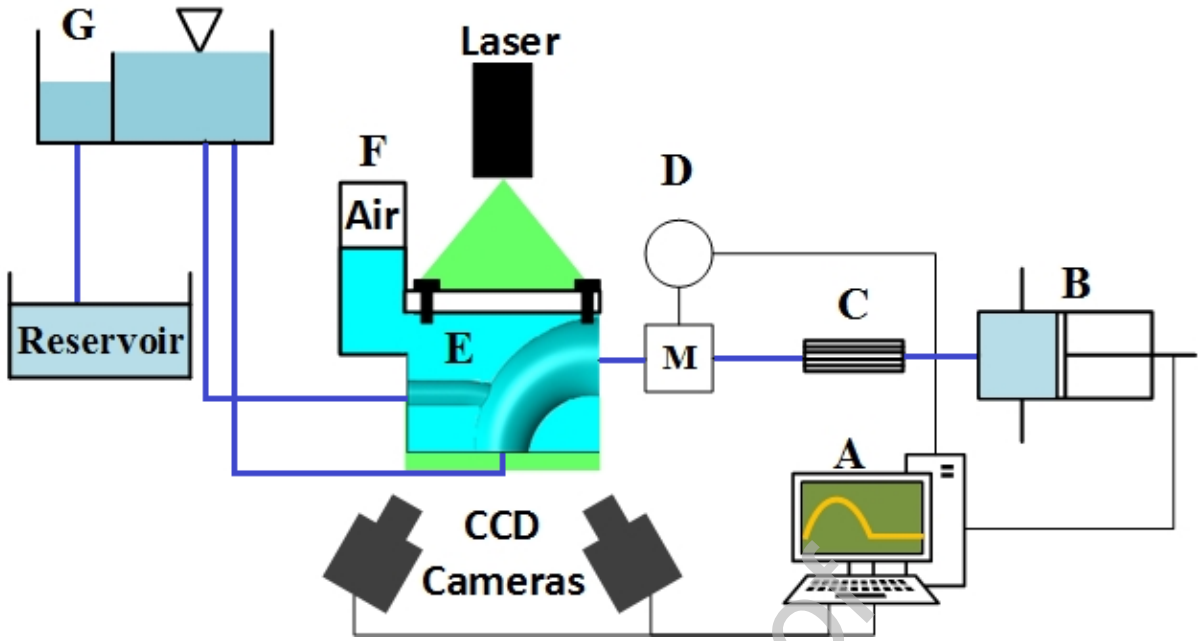


***Fig. 3*** *Experimental fluid circuit setup: (A) data acquisition system , (B) piston pump, (C) flow straightener , (D) electromagnetic flowmeter, (E) pressure box, (F) compliance chamber. The thick blue lines are representative of the flow path, and thin black lines indicate electric signals.*

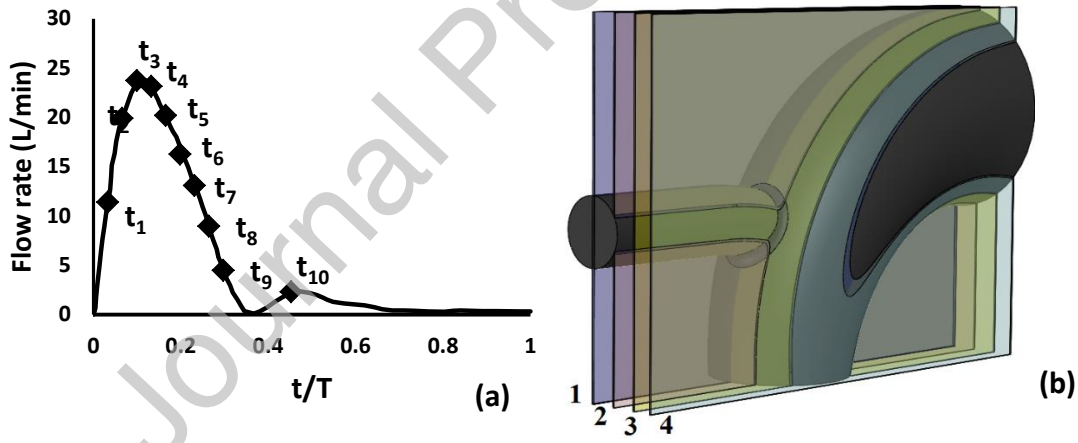


***Fig. 4*** *(a) Normailsed in-vivo inlet physiological flow waveform (b) Schematic view of all measurement plains; the distance between the plain is 5mm.*

Two TSI Powerview 4MP LS PIV cameras (TSI Inc., Shoreview, MN, USA), Scheimpflug adaptors, 60 mm Nikkor lenses, 120 mJ/pulse Nd-YAG laser (New Wave Solo 120 XT) and a 2 mm thick light sheet forming lens train were used in the setup for the stereo-PIV system. The left and right cameras were located 1m from the phantom on a horizontal plane at -30$^{o}$ and +30$^{o}$ from a line perpendicular to the light sheet, respectively. Nominally 10 µm diameter, silver-coated neutrally buoyant hollow glass spheres (Dantec Dynamics S-HGS-10)

seeded the flow. TSI INSIGHT 4G software was used for imaging and processing. Camera calibration was carried out using a TSI dual-plane, 10 mm spacing calibration target. The calibration target was placed in a transparent box filled with the working fluid. Equal refractive angles were achieved by ensuring that the distance between the light sheet and the front face of the box remained consistent across both compliant and rigid models. All key flow dynamics were well captured.

Pre-processing comprised of a disparity correction, subtraction of an average intensity background and static masking of the non-fluid domain. A recursive Nyquist grid engine was used for processing. Processing consisted of ensemble averaging of 20 images at each discrete phase and iterative window sizing with the start and final window dimensions of 64x64 and 32x32 pixels respectively. A Gaussian weighting function emphasising the central pixels before FFT correlation conditioned the windows.

Vector statistics were calculated using TSI INSIGHT 4G's in-built algorithms, with an average of 93% valid vectors after cross correlation and a report of satisfactory interpolated vectors for the final 7%. This rate of valid vectors is generally considered high for successful PIV analysis [32].

## 3. Results

The results were obtained for four different lateral planes in the phantoms (Figure 4b). Raw PIV images of the symmetry plane were calibrated and the wall positions for different times on the cardiac cycle were extracted from the average intensity background images of the symmetry plane. Figure 5 shows the expansion and contraction of the arterial wall on the symmetry-plane during the flow cycle. The diameter change at an arbitrarily chosen, but indicative line (Figure 5 line A-B) on the artery cross-section was calculated using a single camera. The camera image was accurate to 1 pixel which corresponds to 46 µm. The diameter of the artery on the line A-B varied approximately 7% of its natural diameter for the duration of the flow cycle.

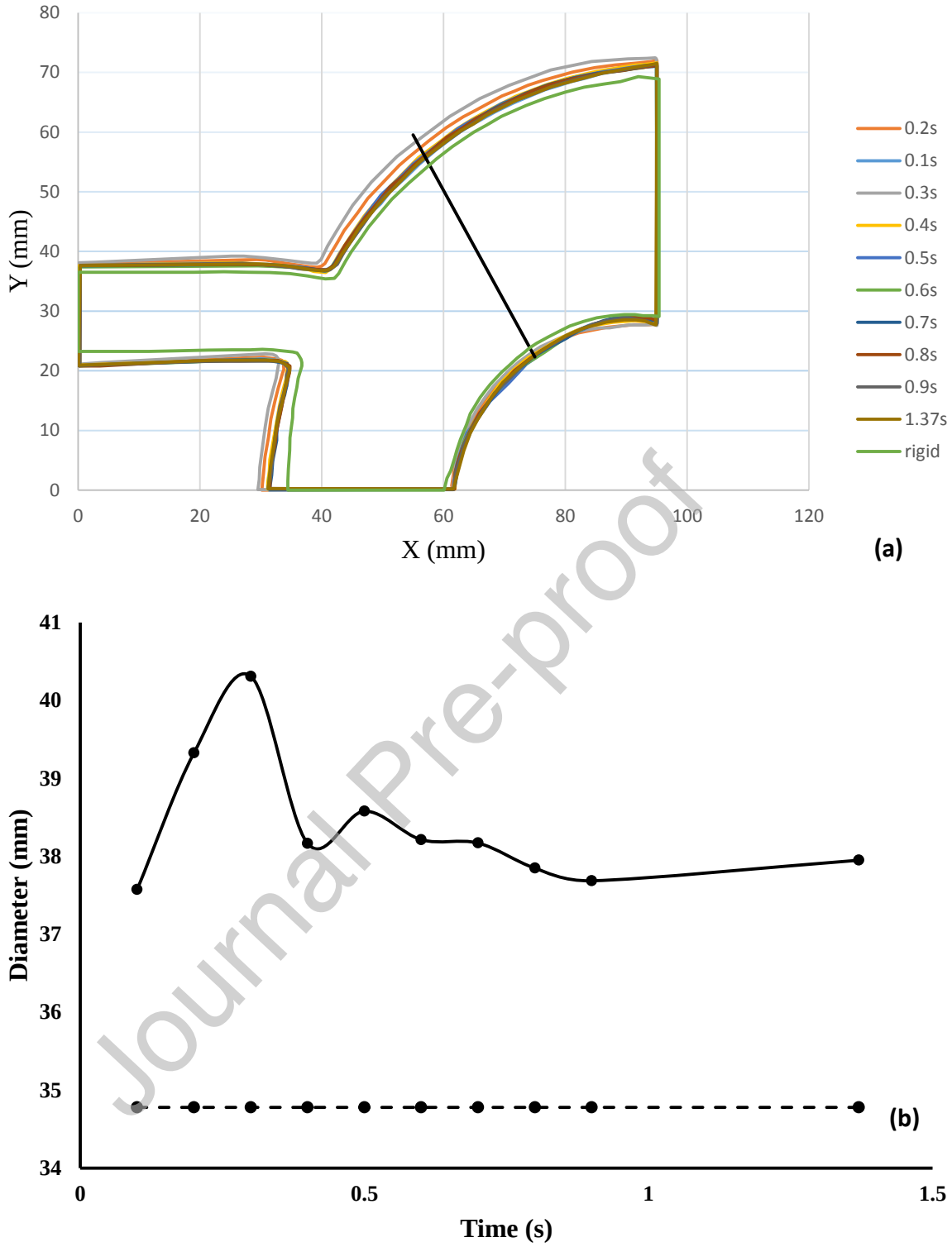




***Fig. 5*** *(a) Wall position change of the compliant and phantom on the symmetry plane. (b) Diameter change of line A-B for compliant (-) and rigid (--) phantom. Note that the flow wave is shown in Figure 4a.*

Figure 6 shows how colour is used to represent in plane velocity in Figures 7 and 8, and opacity is used to show out of plane velocity component. Figure 7 shows the velocity magnitude contour plot of the compliant and rigid phantoms during a cardiac cycle for the central plane. While all flow fields for each measured planes (n=4) at each measured points (n=10) for both phantoms (n=2) in the flow cycle are shown in Appendix A (n=80), only the planes exhibiting interesting or contrasting haemodynamics are presented in this section.

On the symmetry plane during the acceleration phase of systole (*t*=0.1 to 0.3 s), velocity vectors followed the arterial geometry and no evidence of flow separation or backward flow was observed in either the compliant or rigid phantom. These fluid patterns were expected due to high momentum forces and consistent negative pressure gradient during this phase. Velocity magnitude in the BCA of the rigid phantom was approximately double the BCA velocity magnitude in the compliant phantom (Figure 7). Higher velocity in branched arteries of a rigid model was also noticed by Miyazaki, et al. who compared numerical CFD velocity results to MRI obtained velocities [33]. Büsen, Arenz [34] investigated the effects of varying compliance on the flow velocities and vortex formation. As compliance of aortic stiffness reduced, mean velocities were increased and vortex development damped. In contrast to the acceleration phase of systole, during the deceleration of systole (*t*=0.4 to 0.6 s), the general velocity magnitude was higher in the compliant phantom compared to those in the rigid phantom. A low velocity region was initiated at the upper wall of the BCA branch in both phantoms at 0.4s and increased in size as the wave decelerated toward 0.6 s. There were significant differences between the flow in the BCA in the compliant and rigid phantoms. This was one of the regions identified as a high risk point for stenosis formation by Assemat and Siu [5]. While, the rigid phantom had a small recirculation region, the compliant phantom generated a more erratic shape that is indicative of local transitions in velocity. At mid-decelerating systole (t=0.7 s), the compliant phantom showed a large recirculation region in the BCA whereas the rigid phantom exhibited a very small region of recirculation.

At 0.6 s, a flow separation region also formed at the inner wall of the arch in the compliant phantom, which increased in size through the deceleration phase of systole (Appendix A: Velocity Dynamics Figure 10b). This pattern was not observed in the rigid phantom. This was also identified as a risk region for stenosis growth [35]. Two vortices were at 0.8 s and 0.9 s at the distal end of the BCA juncture with the aortic arch for the compliant phantom alone. These recirculation zones may be explained by the reversed flow from the BCA into the aortic arch. There were no observations of such patterns in the rigid model (Figure 7).

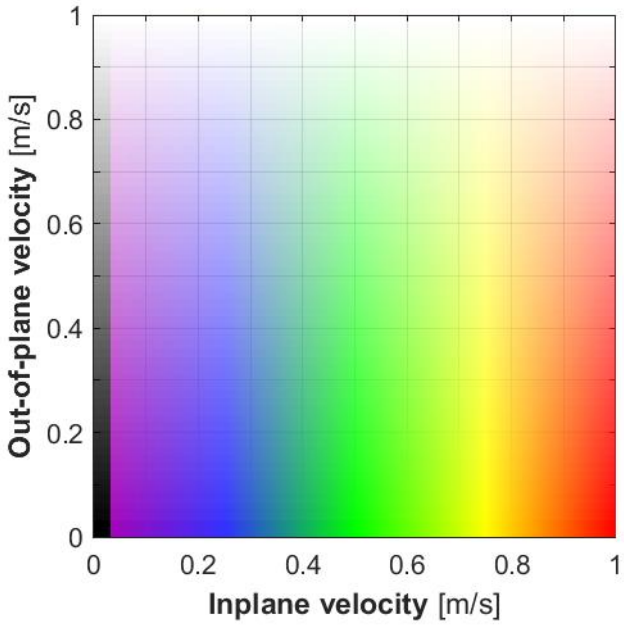


***Fig. 6*** *Legend to enable interpretation of Figures 7 and 8.*

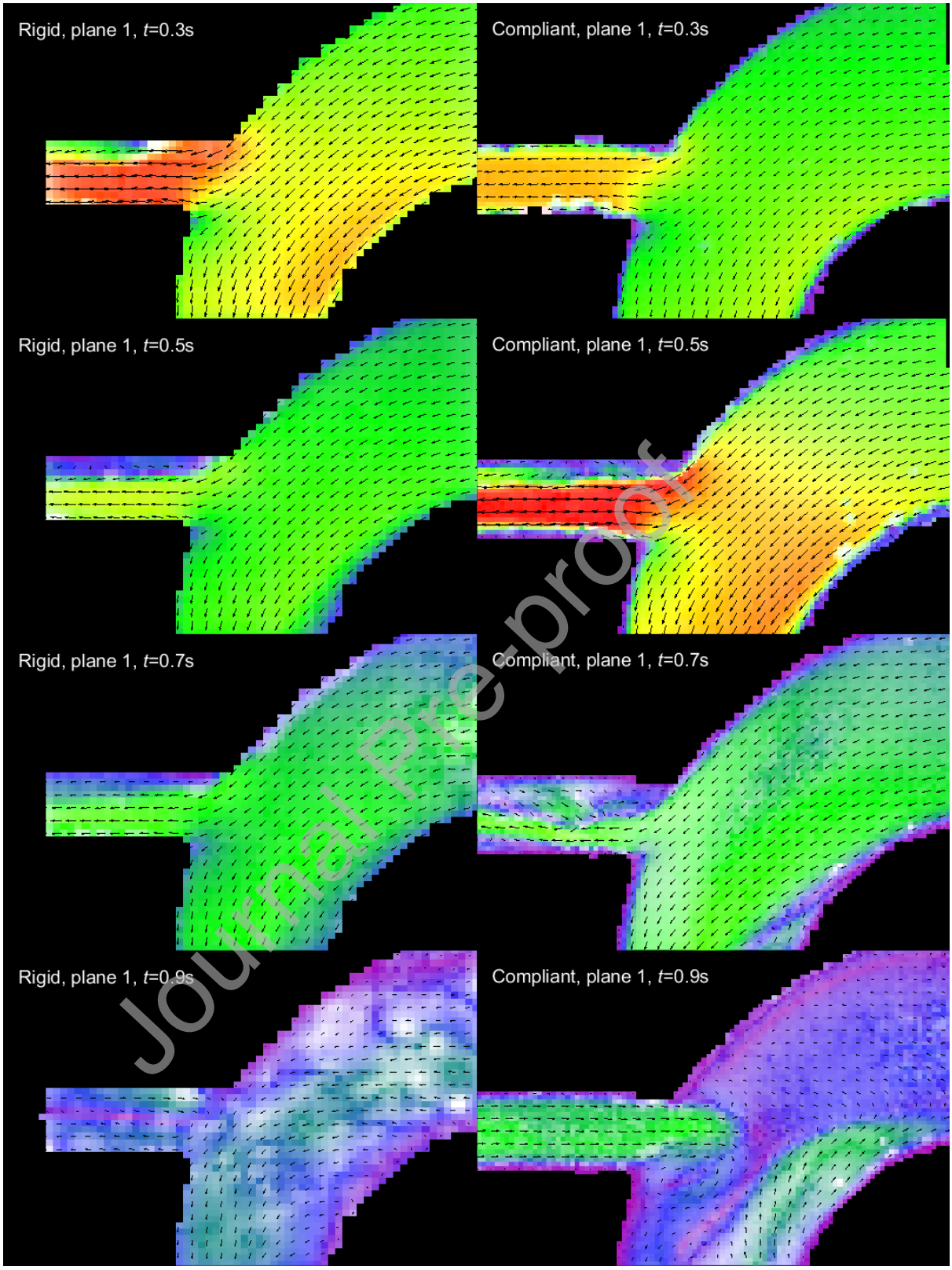


***Fig. 7*** *central plane dynamics at indicative times. All planes and times are shown in the appendix and legend in Figure 6.*

The secondary planes exhibited similar behaviour to the central plane with the exception that lateral out of plane flow was required to conserve mass in the reducing circumference

of the aortic arch. This was most apparent in the BCA during systole (Figure 8). Plane 4 shows vectors that do not comply with the plane boundaries. It is suggested that, while this may not be expected, one must note that the contraction along the aortic geometry could cause significant out of plane flow. Furthermore, the compliant nature of the phantom means that velocity vectors may also have a perpendicular component when the vessel wall is expanding or contracting (rate of displacement of the wall ($V_{wall}$) = 0.01 m/s) (Figure 5). Note that the flow on plane 4 in both phantoms at $t$ = 0.9s tends downwards. This is consistent with the Dean's Vortices shape expected for flow in a curved vessel. However, flow in plane 4 during systole showed no such evidence of this.

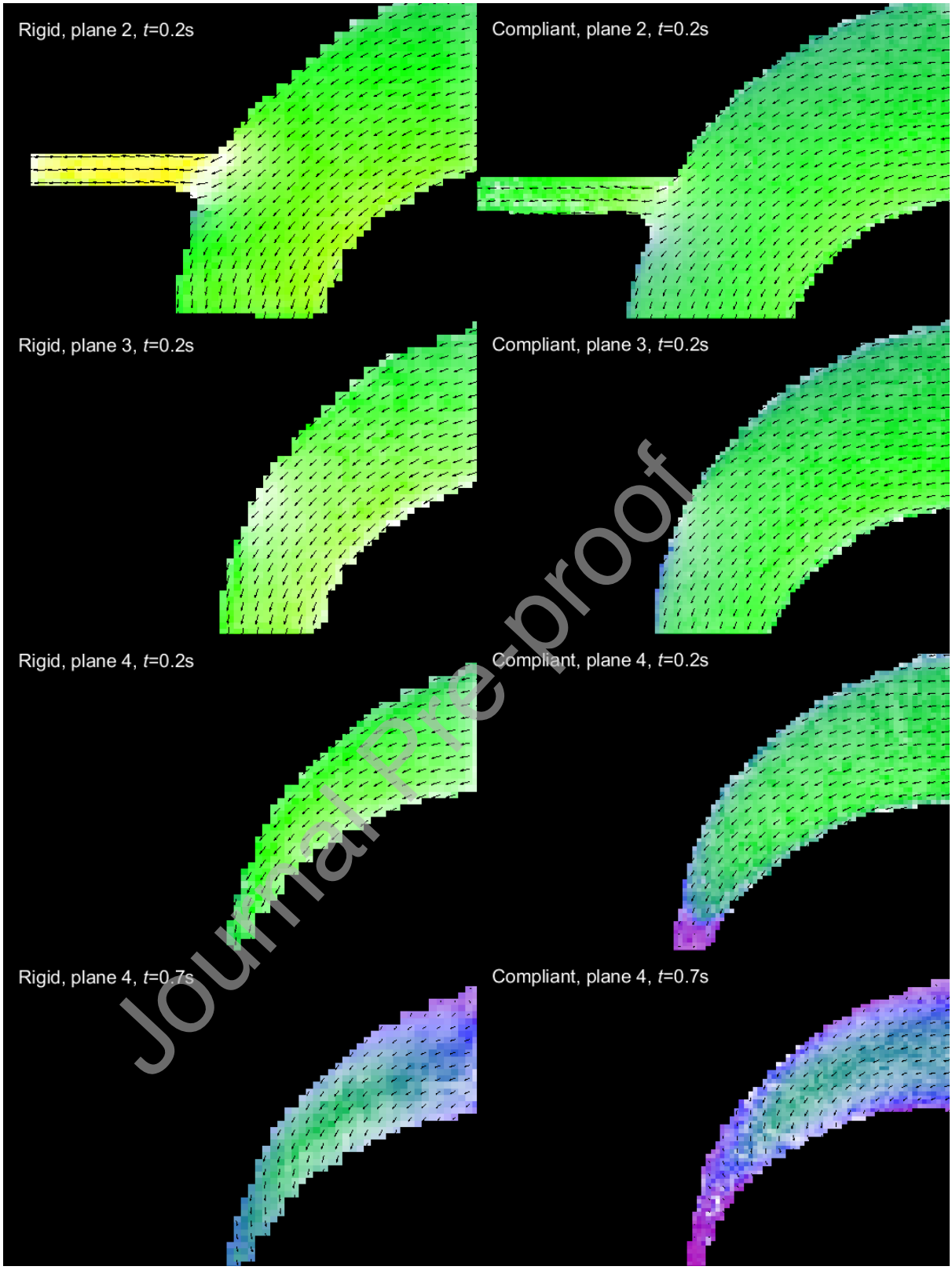


***Fig 8.*** *Non-midplane velocity fields at certain indicative points and velocity scales are shown in Figure 6.*

Figure 9 presents the in-plane shear rate contours (Calculated using PIVview2C (ILA-5150 GmbH, Germany) and plotted in Tecplot 360 (EX 2020 R1)) at t = 0.3 and 0.7 s in the rigid

and compliant phantom. Appendix B contains the shear rate contours for all timesteps. There is a marked difference in shear rate between rigid and compliant phantoms, especially in the BCA. There is a separation of a positive shear layer from the proximal wall of the BCA that occurs during systole. This occurs earlier in the rigid phantom as demonstrate at t = 0.3s. At t= 0.7s, at the location the compliant phantom showed a large recirculation region in the BCA (Figure 7) compared to the rigid, this positive shear layer traversed distally and comes into close proximity to the negative shear observed on the distal wall of the BCA.

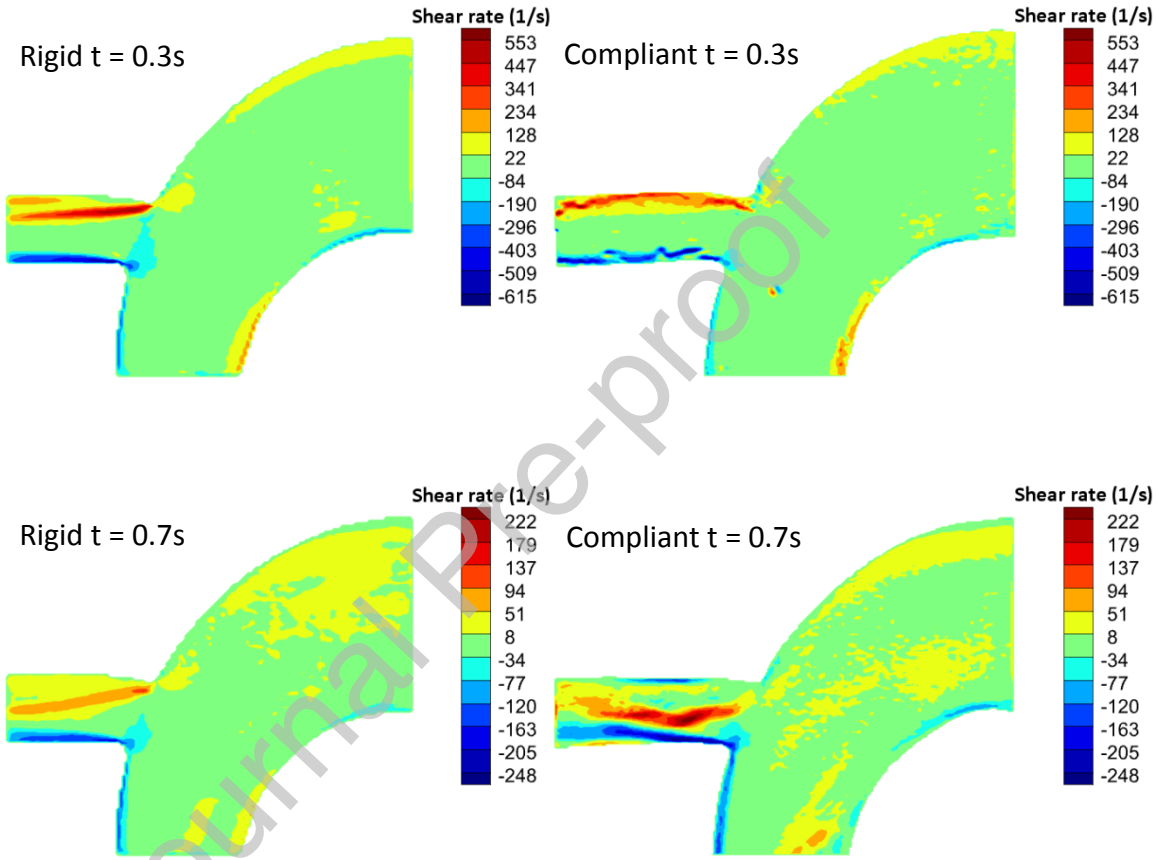


***Fig 9.*** *Shear rate (1/s) contours in the central plane at t= 0.3 and 0.7s.*

## 4. Discussion

The lumen boundary motion of the compliant phantom caused differences in the flow field that are clinically important. In particular, the compliant phantom showed recirculation behaviour in increased atherosclerosis risk regions that was not present in the rigid phantom. The difference between the compliant and rigid results show the importance of fluid-structure interactions in arterial phantoms. A rigid phantom assumption may miss key haemodynamics that have the potential to cause inflammatory responses of cell growth

[36]**.** Recirculation has been noted as a risk factor for the development of stenosis [6-8]. This further supports previous claims that haemodynamic modelling of larger arteries must be undertaken with pulsatile and compliant models [37-40].

During decelerating systole, flow separation and vortices were observed on plane 1 in the proximal BCA region in the compliant phantom but not the rigid phantom (Figure 7). This was coupled with a variation in the observed shear rate. During decelerating systole (*t*=0.4 to 0.6s), the recirculation occurred in the BCA on the edge closer to the heart. This was noted as a key high risk area by Assemat, Siu [5]. The reason for the difference between the flows in the compliant and rigid phantom could potentially be caused by the changing lumen geometry within the compliant phantom. In particular, it may be reasonably assumed that axial stress on the lumen wall will shift the arch in the distal direction and decrease the angle between the BCA and the aortic arch (Angle of red line in Figure 2c becomes more acute) – thus potentially causing the larger recirculation region due to a more pronounced leading edge promoting separation. However, this change in geometry was not quantified. Canstein, et al. suggested that fluid structure interactions may affect normal and pathological blood flow characteristics [14]. Further research is required to determine if this occurs *in-vivo* or if some patient morphologies are more susceptible to this recirculation.

At late decelerating systole, the vortices occurred on the distal region of the juncture between the aortic arch and the BCA in the compliant phantom. These vortices were caused by reversed flow in the BCA entering the aortic arch. This is most likely to have occurred in the compliant phantom as the flow momentum after the flow had ceased at the inlet would have drawn fluid from the aortic arch to the BCA and the distal end of the aortic arch. This would cause low pressure at the proximal end of the aortic arch that would be corrected by low rates of reversed flow during late systole. The rigid phantom would have had the same effect, but due to the relative incompressibility of the working fluid, the reduction of the fluid momentum would have occurred quicker and would not have enabled the reversed flow. The reversed flow in the aortic arch during late decelerating systole, observed only in the compliant phantom, is in another risk region for stenosis development [41]. This important distinction across the rigid and phantom flow patterns further emphasises the importance of the compliant boundary condition. A rigid aortic model is not realistic and may miss important haemodynamic behaviour Further investigation should be made however to ascertain what affect the rigid/compliant boundary interface at the inlet has on this observed reversed flow .

The regions of recirculation and flow separation observed in the compliant phantom at the BCA branch and inner wall of the arch is indicative of reverse flow, intermittent flow, and low WSS. These flow patterns are risk factors for CVD particularly when proximal to the lumen wall as they lead to plaque formation [25, 42-48]. Hence, the accurate identification of the occurrence of aberrations in WSS is critical for *in-vitro* studies to yield clinically

meaningful results. The correlation between the regions of recirculation found in this study and the high risk regions for stenosis formation determined in an *ex-vivo* rat model by Assemat, Armitage [49] does not necessarily enable a comprehensive proof of the model efficacy. However, the phenomenological equivalence across the studies with significant differences in design offers a degree of confidence in the ability of the compliant modelling approach to yield clinically meaningful results.

This study chose to use an idealized geometry. This ensured accurate manufacturing of the phantom and thus, accurate fluid boundary interactions. However, this choice led to several trade-offs. The aorta has out-of-plane curvature which was ignored in this study. This out-of-plane curvature may increase the flow helicity and reduce development of secondary or disturbed flows with disturbed or low WSS. Cunnane, Cunnane [50] investigated the effect of anastomosis angle on helical flow and area of suppressed shear. They reported that out of plane anastomosis curvature angle can increase the helical flow and reduce distribution of low/oscillating WSS. There was also a slight increase in resting diameter of the compliant model compared to the rigid due to fluid pressure. Future work may look to offset this in the phantom manufacture process. Additionally, the absence of the tricuspid valve would lead to an unphysiological flow into the aortic arch. This would be likely to affect the proximal flow region – particularly in systole. However, this region was generally free from flow patterns that might imply WSS aberrations *in-vivo.* Thus, the concern was limited. It should also be noted that the flow rate in the BCA was not controlled or directly measured. A constant head pressure downstream of the flow circuit provided the same back pressure for both BCA and the aortic arch. Future work may control the head pressures of the BCA and aortic arch individually to understand any affect this may have.

It may also be reasonable to question why atherosclerosis is not more prevalent given relatively high-risk flow properties observed in this model of relatively healthy geometry and flow properties. There are two factors that have to be considered. Firstly, the out of plane curvature of an *in-vivo* aorta will lead to a washout of recirculation as a result of helical flow. Secondly, the level of oxLDL (oxidised low density lipoprotein) is also a determinant of plaque formation and is greatly affected by diet, gender and age [51-53]. Macrophage cells absorb oxLDL and generally have higher densities in these at risk regions [54, 55]. Progressive absorption of oxLDL results in generation of foam cells [56] that stick to arterial lumen, damage the endothelium cells and ultimately lead to symptomatic CVD.

The similarity of flow patterns on the different measurement planes show the redundancy of undertaking PIV measurement for these planes. However, this study aimed to determine the flow patterns within the aorta and ultimately determined that for this particular geometry, there were no major flow patterns off the central plane that did not also exist on the central plane. There was some indication of Dean's vortices. In particular, the flow tended distal on the off central planes and was slightly straighter in the central plane.

However, it seems that the nature of the pulsatile flow in the compliant phantom, and the geometry of the BCA prevented the establishment of strong Dean's vortices. Dean's vortices are driven by the different level of momentum in the central flow compared to the peripheral flow in a curved vessel. An increased Dean Number results in development of a stronger secondary flow. This secondary flow creates two counter-rotating flows transverse to the dominant flow direction and may lead to flow separation at high Dean numbers [57]. However, much of this flow is directed into the BCA and thus fails to recirculate around the peripheral regions. Therefore, matching the observed Dean number with the Dean number expected for a rigid aortic geometry with a BCA would not be informative. Furthermore, during diastole, the flow in the BCA is limited and establishment of weak vortices seems to occur. Overall, the out of plane flow, and flow fields off the central plane of the in-vitro model did not exhibit any clinically important dynamics.

This study compared the haemodynamic flow fields generated by compliant and rigid phantoms of the ascending aorta arch and BCA and found significant differences across the haemodynamics across the models. The differences were most prominent in regions of the arterial wall that have been noted as high risk regions for plaque deposition and the onset of CVD. The outcomes of the study support previous findings that show pulsatile flow and compliant models are necessary when assessing haemodynamic flows. This study showed how haemodynamics in the aortic arch are heavily influenced by the compliance of the arterial structure. This has implications for the design and *in-vitro* testing of implant design. In particular, *in-vivo* animal studies limit observability of deleterious flow behaviours, and rigid *in-vitro* or *in-silico* can lack important flow features. Hence, compliant *in-vitro* studies should be used when informative observation of flow patterns is required. Hence, the design of *in-vitro* or *in-silico* haemodynamic experiments should incorporate physiological fluid-boundary interactions to maximise clinical insight and relevance.

An ideal phantom geometry was used in this study, while the *in-vivo* geometry of aortic arch has out of plane tortuosity which may induce flow helicity. While this study could not capture such a flow behaviour, the aim was to provide general understanding of the flow phenomena at this arterial region. The flow loop did not include a tricuspid valve and used a flow straighter leading to a developed flow at inlet. It is suggested in future studies that this should be incorporated to elucidate the affect it has on the flow field.

## 6. Acknowledgements

Competing interests: None declared

Sina G Yazdi was supported during this research by the University of Canterbury Doctoral Scholarship scheme.

Ethical approval: Not required

# 7. References

[1] WHO WHO. Cardiovascular diseases (CVDs): Fact sheet No. 317. 2012. Geneva: World Health Organization Google Scholar. 2012.

[2] Stoner L, Sabatier MJ. Use of ultrasound for non-invasive assessment of flow-mediated dilation. Journal of atherosclerosis and thrombosis. 2012;19:407-21.

[3] Cecchi E, Giglioli C, Valente S, Lazzeri C, Gensini GF, Abbate R, et al. Role of hemodynamic shear stress in cardiovascular disease. Atherosclerosis. 2011;214:249-56.

[4] Mazumdar JN. Biofluid Mechanics. World Scientific, Singapore. 1992.

[5] Assemat P, Siu KK, Armitage JA, Hokke SN, Dart A, Chin-Dusting J, et al. Haemodynamical stress in mouse aortic arch with atherosclerotic plaques: Preliminary study of plaque progression. Computational and structural biotechnology journal. 2014;10:98-106.

[6] Poepping TL, Rankin RN, Holdsworth DW. Flow patterns in carotid bifurcation models using pulsed Doppler ultrasound: effect of concentric vs. eccentric stenosis on turbulence and recirculation. Ultrasound in medicine & biology. 2010;36:1125-34.

[7] Bluestein D, Niu L, Schoephoerster RT, Dewanjee MK. Fluid mechanics of arterial stenosis: relationship to the development of mural thrombus. Annals of biomedical engineering. 1997;25:344.

[8] Pritchard WF, Davies PF, Derafshi Z, Polacek DC, Tsao R, Dull RO, et al. Effects of wall shear stress and fluid recirculation on the localization of circulating monocytes in a three-dimensional flow model. Journal of biomechanics. 1995;28:1459-69.

[9] Bulusu KV, Plesniak MW. Experimental Investigation of Secondary Flow Structures Downstream of a Model Type IV Stent Failure in a 180° Curved Artery Test Section. Journal of visualized experiments: JoVE. 2016.

[10] Mokhtar NH, Abas A, Razak N, Hamid MNA, Teong SL. Effect of different stent configurations using Lattice Boltzmann method and particles image velocimetry on artery bifurcation aneurysm problem. Journal of theoretical biology. 2017;433:73-84.

[11] Chung B, Cebral JR. CFD for Evaluation and Treatment Planning of Aneurysms: Review of Proposed Clinical Uses and Their Challenges. Annals of Biomedical Engineering. 2015;43:122-38.

[12] Shimogaito K, Ohara K, Ichikawa A, Kubo T, Fukuda T. The study of valved hybrid fractal stent for the next generation medical care—The blood flow simulation in cerebral aneurysm by CFD. Micro-NanoMechatronics and Human Science (MHS), 2016 International Symposium on: IEEE; 2016. p. 1-3.

[13] Chen Z, Jena SK, Giridharan GA, Koenig SC, Slaughter MS, Griffith BP, et al. Flow features and device-induced blood trauma in CF-VADs under a pulsatile blood flow condition: A CFD comparative study. International journal for numerical methods in biomedical engineering. 2017.

[14] Canstein C, Cachot P, Faust A, Stalder AF, Bock J, Frydrychowicz A, et al. 3D MR flow analysis in realistic rapid-prototyping model systems of the thoracic aorta: Comparison with in vivo data and computational fluid dynamics in identical vessel geometries. Magnetic Resonance in Medicine. 2008;59:535-46.

[15] Deplano V, Guivier-Curien C, Bertrand E. 3D analysis of vortical structures in an abdominal aortic aneurysm by stereoscopic PIV. Experiments in Fluids. 2016;57:167.

[16] Ionita CN, Hoi Y, Meng H, Rudin S. Particle image velocimetry (PIV) evaluation of flow modification in aneurysm phantoms using asymmetric stents. Medical Imaging 2004: International Society for Optics and Photonics; 2004. p. 295-306.

[17] Kefayati S, Milner JS, Holdsworth DW, Poepping TL. In vitro shear stress measurements using particle image velocimetry in a family of carotid artery models: effect of stenosis severity, plaque eccentricity, and ulceration. PloS one. 2014;9:e98209.

[18] Minakawa M, Fukuda I, Igarashi T, Fukui K, Yanaoka H, Inamura T. Hydrodynamics of aortic cannulae during extracorporeal circulation in a mock aortic arch aneurysm model. Artificial organs. 2010;34:105-12.

[19] Scardulla F, Bellavia D, D'Acquisto L, Raffa GM, Pasta S. Particle image velocimetry study of the celiac trunk hemodynamic induced by continuous-flow left ventricular assist device. Medical Engineering & Physics. 2017;47:47-54.
[20] Pasta S, Scardulla F, Rinaudo A, Raffa GM, D'Ancona G, Pilato M, et al. An In Vitro Phantom Study on the Role of the Bird-Beak Configuration in Endograft Infolding in the Aortic Arch. 2016;23:172-81.
[21] Anayiotos AS, Jones SA, Giddens DP, Glagov S, Zarins CK. Shear Stress at a Compliant Model of the Human Carotid Bifurcation. Journal of Biomechanical Engineering. 1994;116:98-106.
[22] Reymond P, Crosetto P, Deparis S, Quarteroni A, Stergiopulos N. Physiological simulation of blood flow in the aorta: Comparison of hemodynamic indices as predicted by 3-D FSI, 3-D rigid wall and 1-D models. Medical Engineering and Physics. 2013;35:784-91.
[23] Geoghegan PH, Jermy MC, Nobes DS. A PIV Comparison of the Flow Field and Wall Shear Stress in Rigid and Compliant Models of Healthy Carotid Arteries. Journal of Mechanics in Medicine and Biology. 2017;17:1750041.
[24] Docherty PD, Geoghegan PH, Huetter L, Jermy M, Sellier M. Regressive cross-correlation of pressure signals in the region of stenosis: Insights from particle image velocimetry experimentation. Biomedical Signal Processing and Control. 2017;32:143-9.
[25] Yazdi SG, Geoghegan PH, Docherty PD, Jermy M, Khanafer A. A Review of Arterial Phantom Fabrication Methods for Flow Measurement Using PIV Techniques. Annals of Biomedical Engineering. 2018;46:1697-721.
[26] Hütter L, Geoghegan PH, Docherty PD, Lazarjan MS, Clucas D, Jermy M. Fabrication of a compliant phantom of the human aortic arch for use in Particle Image Velocimetry (PIV) experimentation. Current Directions in Biomedical Engineering. 2016;2:493-7.
[27] Geoghegan P, Buchmann N, Spence C, Moore S, Jermy M. Fabrication of rigid and flexible refractive-index-matched flow phantoms for flow visualisation and optical flow measurements. Experiments in fluids. 2012;52:1331-47.
[28] Geoghegan PH, Buchmann NA, Soria J, Jermy MC. Time-resolved PIV measurements of the flow field in a stenosed, compliant arterial model. Experiments in Fluids. 2013;54:1528.
[29] Yazdi SG, Huetter L, Docherty PD, Williamson PN, Clucas D, Jermy M, et al. A Novel Fabrication Method for Compliant Silicone Phantoms of Arterial Geometry for Use in Particle Image Velocimetry of Haemodynamics. Applied Sciences. 2019;9:3811.
[30] Stalder A, Russe M, Frydrychowicz A, Bock J, Hennig J, Markl M. Quantitative 2D and 3D phase contrast MRI: optimized analysis of blood flow and vessel wall parameters. Magnetic resonance in medicine. 2008;60:1218-31.
[31] Shahcheraghi N, Dwyer H, Cheer A, Barakat A, Rutaganira T. Unsteady and three-dimensional simulation of blood flow in the human aortic arch. Journal of biomechanical engineering. 2002;124:378-87.
[32] Lu L, Sick V. High-speed particle image velocimetry near surfaces. J Vis Exp. 2013:50559.
[33] Miyazaki S, Itatani K, Furusawa T, Nishino T, Sugiyama M, Takehara Y, et al. Validation of numerical simulation methods in aortic arch using 4D Flow MRI. Heart and Vessels. 2017;32:1032-44.
[34] Büsen M, Arenz C, Neidlin M, Liao S, Schmitz-Rode T, Steinseifer U, et al. Development of an In Vitro PIV Setup for Preliminary Investigation of the Effects of Aortic Compliance on Flow Patterns and Hemodynamics. Cardiovasc Eng Tech. 2017;8:368-77.
[35] Won D, Zhu S-N, Chen M, Teichert A-M, Fish JE, Matouk CC, et al. Relative reduction of endothelial nitric-oxide synthase expression and transcription in atherosclerosis-prone regions of the mouse aorta and in an in vitro model of disturbed flow. The American journal of pathology. 2007;171:1691-704.
[36] Lantz J, Renner J, Karlsson MJIJoAM. Wall shear stress in a subject specific human aorta—influence of fluid-structure interaction. 2011;3:759-78.

[37] Jin S, Oshinski J, Giddens DP. Effects of wall motion and compliance on flow patterns in the ascending aorta. Journal of biomechanical engineering. 2003;125:347-54.
[38] Chandra S, Raut SS, Jana A, Biederman RW, Doyle M, Muluk SC, et al. Fluid-structure interaction modeling of abdominal aortic aneurysms: the impact of patient-specific inflow conditions and fluid/solid coupling. Journal of biomechanical engineering. 2013;135:081001.
[39] Liu X, Fan Y, Deng X, Zhan F. Effect of non-Newtonian and pulsatile blood flow on mass transport in the human aorta. Journal of biomechanics. 2011;44:1123-31.
[40] DeGroff CG, Orlando W, Shandas R. Insights into the effect of aortic compliance on Doppler diastolic flow patterns seen in coarctation of the aorta: a numeric study. Journal of the American Society of Echocardiography. 2003;16:162-9.
[41] Hahn C, Schwartz MA. Mechanotransduction in vascular physiology and atherogenesis. Nature reviews Molecular cell biology. 2009;10:53.
[42] Meng H, Tutino V, Xiang J, Siddiqui A. High WSS or low WSS? Complex interactions of hemodynamics with intracranial aneurysm initiation, growth, and rupture: toward a unifying hypothesis. American Journal of Neuroradiology. 2014;35:1254-62.
[43] Rouleau L, Rossi J, Leask RL. The Response of Human Aortic Endothelial Cells in a Stenotic Hemodynamic Environment: Effect of Duration, Magnitude, and Spatial Gradients in Wall Shear Stress. Journal of Biomechanical Engineering. 2010;132:071015--11.
[44] Traub O, Berk BC. Laminar shear stress: mechanisms by which endothelial cells transduce an atheroprotective force. Arteriosclerosis, thrombosis, and vascular biology. 1998;18:677-85.
[45] da Conceicao Pereira G, Krams R. 182 Flow Characteristics Enhanced by the Compliant Arteries and their effects in Vulnerable Plaque Formation. BMJ Publishing Group Ltd and British Cardiovascular Society; 2015.
[46] Kabinejadian F, Cui F, Su B, Danpinid A, Ho P, Leo HL. Effects of a carotid covered stent with a novel membrane design on the blood flow regime and hemodynamic parameters distribution at the carotid artery bifurcation. Medical & Biological Engineering & Computing. 2015;53:165-77.
[47] Morbiducci U, Kok AM, Kwak BR, Stone PH, Steinman DA, Wentzel JJ. Atherosclerosis at arterial bifurcations: evidence for the role of haemodynamics and geometry. Thromb Haemost. 2016;115:484-92.
[48] Wentzel JJ, Chatzizisis YS, Gijsen FJ, Giannoglou GD, Feldman CL, Stone PH. Endothelial shear stress in the evolution of coronary atherosclerotic plaque and vascular remodelling: current understanding and remaining questions. Cardiovascular research. 2012;96:234-43.
[49] Assemat P, Armitage JA, Siu KK, Contreras KG, Dart AM, Chin-Dusting JP, et al. Three-dimensional numerical simulation of blood flow in mouse aortic arch around atherosclerotic plaques. Applied Mathematical Modelling. 2014;38:4175-85.
[50] Cunnane CV, Cunnane EM, Moran DT, Walsh MT. The presence of helical flow can suppress areas of disturbed shear in parameterised models of an arteriovenous fistula. 2019;35:e3259.
[51] Head T, Daunert S, Goldschmidt-Clermont PJ. The aging risk and atherosclerosis: a fresh look at arterial homeostasis. Frontiers in genetics. 2017;8:216.
[52] Liao D-F, Jin Z-G, Baas AS, Daum G, Gygi SP, Aebersold R, et al. Purification and identification of secreted oxidative stress-induced factors from vascular smooth muscle cells. Journal of Biological Chemistry. 2000;275:189-96.
[53] Hao W, Friedman A. The LDL-HDL profile determines the risk of atherosclerosis: a mathematical model. PloS one. 2014;9:e90497.
[54] Moore KJ, Sheedy FJ, Fisher EA. Macrophages in atherosclerosis: a dynamic balance. Nature Reviews Immunology. 2013;13:709.
[55] Miller YI, Choi S-H, Fang L, Tsimikas S. Lipoprotein modification and macrophage uptake: role of pathologic cholesterol transport in atherogenesis. Cholesterol Binding and Cholesterol Transport Proteins:: Springer; 2010. p. 229-51.

[56] Holvoet P, Kritchevsky SB, Tracy RP, Mertens A, Rubin SM, Butler J, et al. The metabolic syndrome, circulating oxidized LDL, and risk of myocardial infarction in well-functioning elderly people in the health, aging, and body composition cohort. Diabetes. 2004;53:1068-73.
[57] Ku DN. Blood flow in arteries. Annual Review of Fluid Mechanics. 1997;29:399-434.